TECHNICAL ARTICLE

# Effect of Weaving on Fe$_3$Al Layers Prepared by Arc Deposition Technique

Jingyu Zhao, Guoxiang Xu, Zan Wang, Jia Ju, Xianli Wang, Mingzhi Chen, Feng Xue, and Jian Zhou

Fe$_3$Al combines with steel to form bimetallic metal can benefit from steel's mechanical strength and make full use of Fe$_3$Al's excellent performance under high temperatures. However, due to the poor fluidity and wettability of liquid Fe$_3$Al to steel, the cladding prepared by traditional linear welding is not available to industrial sector. Hence, to optimize preparation, an arc deposition procedure based on a weaving path is proposed. Fe$_3$Al cladding was prepared on the steel with weaving and linear paths by arc deposition technology, respectively, and the characteristics of the cladding were compared in terms of formability, surface feature and microstructure. The results demonstrated that the cladding prepared by weave arc deposition had better formability, lower dilution rates and fewer defects than that by the line one. Compared with the image captured by high-speed camera, the substantial difference was attributed to the higher molten pool velocities, which led to a smaller volume of molten pool in weave process. Under this circumstance, the arc force was conducive to the spread of liquid metal, forming a relatively small contact angle ($< 45°$). The finite element analysis revealed that the temperature distribution and thermal cycles resulted in finer grains in the weave process; furthermore, the weave process produced less residual stress, causing an increment of 153% in bonding strength between the cladding and the steel, compared to linear sample. Overall, the weave arc deposition technology is capable of molding Fe$_3$Al layers efficiently and offers a good prospect for applications.

## 1. Introduction

Fe$_3$Al-based iron aluminide intermetallic compounds have been extensively investigated because of their excellent properties such as oxidation resistance, vulcanization resistance and erosion resistance at high temperatures (Ref 1-3). Combined with the advantages of low density and low material cost, Fe$_3$Al intermetallic compounds are likely to replace special alloy steels to be applied in harsh thermal and corrosive environments (Ref 4, 5).

At present, due to the brittleness of Fe$_3$Al alloys at room temperature and low strength at high temperature, its industrial application is limited (Ref 6). In recent years, a lot of effort has been paid to improving the mechanical properties of Fe$_3$Al alloy. Therein adding alloying elements including boron, chromium, cerium, carbon, niobium and titanium can improve the ductility of Fe$_3$Al alloy at room temperature (Ref 7-10), and

Jingyu Zhao, Zan Wang, Xianli Wang, Feng Xue, and Jian Zhou, School of Materials Science and Engineering, Southeast University, Nanjing 211189, China; Guoxiang Xu, School of Materials Science and Engineering, Jiangsu University of Science and Technology, Zhenjiang 212003, China; Jia Ju, Jiangsu Key Laboratory of Advanced Structural Materials and Application Technology, Nanjing Institute of Technology, Nanjing 211167, China; and Mingzhi Chen, School of Mechanical Engineering, Southeast University, Nanjing 211189, China. Contact e-mail: jethro@seu.edu.cn.

Kratochvil et al. (Ref 11) added zirconium to improve the mechanical properties at high temperatures. However, these studies have not made a fundamental breakthrough, and the production and processing of Fe$_3$Al alloys still have many problems (Ref 12). Therefore, as a high-temperature industrial structural material, Fe$_3$Al has not yet been widely applied.

Shen et al. (Ref 13) proved that the Fe$_3$Al/steel bimetal composite can provide a range of complementary advantages, such as excellent strength and plasticity provided by the steel substrate, and superior surface properties provided by the Fe$_3$Al layer. The preparation of this bimetallic material will be highly economic and will also allow for increased application possibilities for iron aluminide in high-temperature environments, such as in the electric power industry, petroleum industry and chemical industry (Ref 14).

The latest research on the combination of Fe$_3$Al and steel has focused on additive manufacturing of Fe$_3$Al on steel substrates (Ref 15-17), dissimilar welding between Fe$_3$Al and steel (Ref 18), and preparation of Fe$_3$Al cladding layers on steel plates (Ref 19). The Fe$_3$Al layer is made by surfacing welding (Ref 16), plasma spraying (Ref 20), cold spraying (Ref 21), laser cladding (Ref 22) and other processes. Samples produced by these processes usually have some defects, such as cracks, low density, poor surface molding and high porosity.

Yang et al. (Ref 23) introduced arc deposition technology is a method of arc welding and is characterized by less spatter and less heat input. In recent years, arc deposition technology has been widely used in the manufacture of nickel-based alloys, aluminum alloys, magnesium alloys and copper alloy deposits (Ref 24-27), and may be a promising method for producing high-quality Fe$_3$Al-deposited layers on steel plates. However, high brittleness at room temperature, low thermal conductivity,

great changes of thermal expansion coefficient from low temperature to high temperature, as well as poor melt fluidity of $Fe_3Al$ (Ref 22), those unfavorable combinations of factors result in the poor formability of the cladding (Ref 28), such as large thickness, small width of layer and serious dilution. Additionally, due to the large thermal stress, cracks are likely to occur on the surface of $Fe_3Al$-deposited layer. Moreover, on account of the inherent brittleness of $Fe_3Al$, its wire is difficult to be manufactured by extrusion and drawing (Ref 19). Therefore, the cladding prepared by traditional linear welding is not available in actual production process, and there are few studies on the use of arc deposition technology to prepare $Fe_3Al$ deposition layers on steel.

To overcome the poor performance and optimize preparation, an arc deposition procedure based on a weaving path is proposed. This study aims to prepare $Fe_3Al$ cladding with good formability used by arc deposition technology. The traditional preparation based on a linear path was conducted to make a comparison. The influences of these two approaches on the morphology, formability and microstructure of the cladding were studied. A high-speed camera was used to capture the molten pool images in the formation process, in addition, to explain the formation of microstructure more accurately, a three-dimensional model was established and computed by a finite element analysis computer technology, the temperature field in cladding during the arc deposition in line and weave way were compared and discussed.

## 2. Materials and Methods

### 2.1 Arc Deposition Experiment

The $Fe_3Al$ deposition layer was prepared using $Fe_3Al$ flux-cored wire rather than traditional solid-core wire with a diameter of 1.6 mm, as shown in Fig. 1(d). Its structure was iron sheet coated with aluminum powder, which was made by multiple drawings; the purpose of this preparation was to avoid that $Fe_3Al$ solid-core wire was too brittle to be drawn into wire (Ref 19). The substrate was a Q235 steel plate with a thickness of 3 mm. The chemical composition of the welding wire and steel plate is shown in Table 1. The power supply for arc deposition was a Yaskawa model RD350, and the cabinet for the control was a Yaskawa model DX200. The MA1440 six-axis arc welding robot was implemented for the arc deposition experiment. The shielding gas was pure Ar with a flow rate of 20 L/min. During the production of arc deposition, the $Fe_3Al$ welding wire was first melted to form droplets under the high-temperature arc, then the droplet was merged into the molten pool under the action of multiple forces, and then, the molten pool was moved with the movement of the welding torch; finally, a cladding of $Fe_3Al$ was formed on the steel plate after the molten pool was solidified. The temperature measurement was taken by using K-type thermocouples which were fixed at 5 mm from weld toe on the top surface of steel in two approaches. Figure 1(a) and (c) represents a schematic diagram and equipment to understand this operation.

To characterize the droplet transition and molten pool morphology of arc deposition, the high-speed camera was placed parallel to the direction of arc deposition, and the angle between its center line and the steel was 30°. The image acquisition mainly relied on the passive photosensitive method in which the laser light source illuminated the molten pool. The laser light source with a power of 2 W was fixed above the camera, and the angle with the steel was 60°. The model of the high-speed camera was NAC-hx-7s with 3000 fps, the lens focal length was 105 nm, and in addition, an 808 nm filter was installed in front of the lens to filter other interfering light.

Line and weave deposition methods were applied for arc deposition. Three samples were prepared for each deposition method, the only parameter which fluctuated within the process was the current, and it was adjusted by 20 A; the purpose of this fabrication is therefore to compare the experimental results of same heat inputs on the formability and grain morphology between two processes. The process parameters of the arc deposition experiment are listed in Table 2. Due to the particularity of power supply, the wire feeding speed was automatically matched according to the current during arc deposition. In the line arc deposition method, the path is a straight line from the beginning to the end of the arc deposition. In the weaving arc deposition method, from the beginning to the end of the arc deposition, the path advances periodically in a "$W$" shape. The schematic diagrams of the two deposition paths are shown in Fig. 1(b).

The image acquisition of forming appearance and defect inspection operations were carried out after the sample preparation, respectively, and then, a wire-cut electrical discharge machining was employed to obtain the cross section of the samples. The extracted samples, normally, were separated from the middle portion of the cladding, considering it was undergoing a relatively stable stage of arc deposition to avoid being adversely affected by both arc igniting and arc extinguishing. For a smooth surface of cross section, grinding and polishing were performed by an automatic machine that utilized a series of abrasive paper successively: 200 #, 600 #, 1200 #, 1600 # and 2000 #. After grinding and polishing, the sample was etched by aqua regia ($HNO_3$:HCl = 1:3) for 30 s, then sprayed with alcohol to remove any remaining liquid and dried the surface. A metallurgical microscope was used to observe the microstructure of the cladding cross section. The phase composition of the deposited layer was investigated by x-ray diffraction. The hardness was measured on the cross section via a micro-hardness tester. The samples for the bonding strength test were made by wire cutting. A tensile testing machine was used to measure the bonding strength between the deposited layer and the steel substrate at a stress rate of 1 mm/min.

### 2.2 Finite Element Analysis

In order to accurately characterize and explain the experimental consequence, in this study, the temperature field and stress field of two methods were simulated based on FEA. The three-dimensional model was built according to the real size of samples and then meshed; in detail, there were two types of mesh used: the fine mesh near the deposition layer for ensuring the accuracy of the calculation results and the coarse mesh far away from the cladding for saving computation time. Total nodes and elements for weaving method were 6570 and 5280, respectively, while those for line produce were 5940 and 4608. The finite element model and meshing are shown in Fig. 2(a) and (b).

When wires are heated by arc during deposition, the arc heat distribution mode exhibits the characteristics of volumetric heat; thus, the double ellipsoid heat source model is suited to summarize temperature field and the shape of metallic bath (Ref
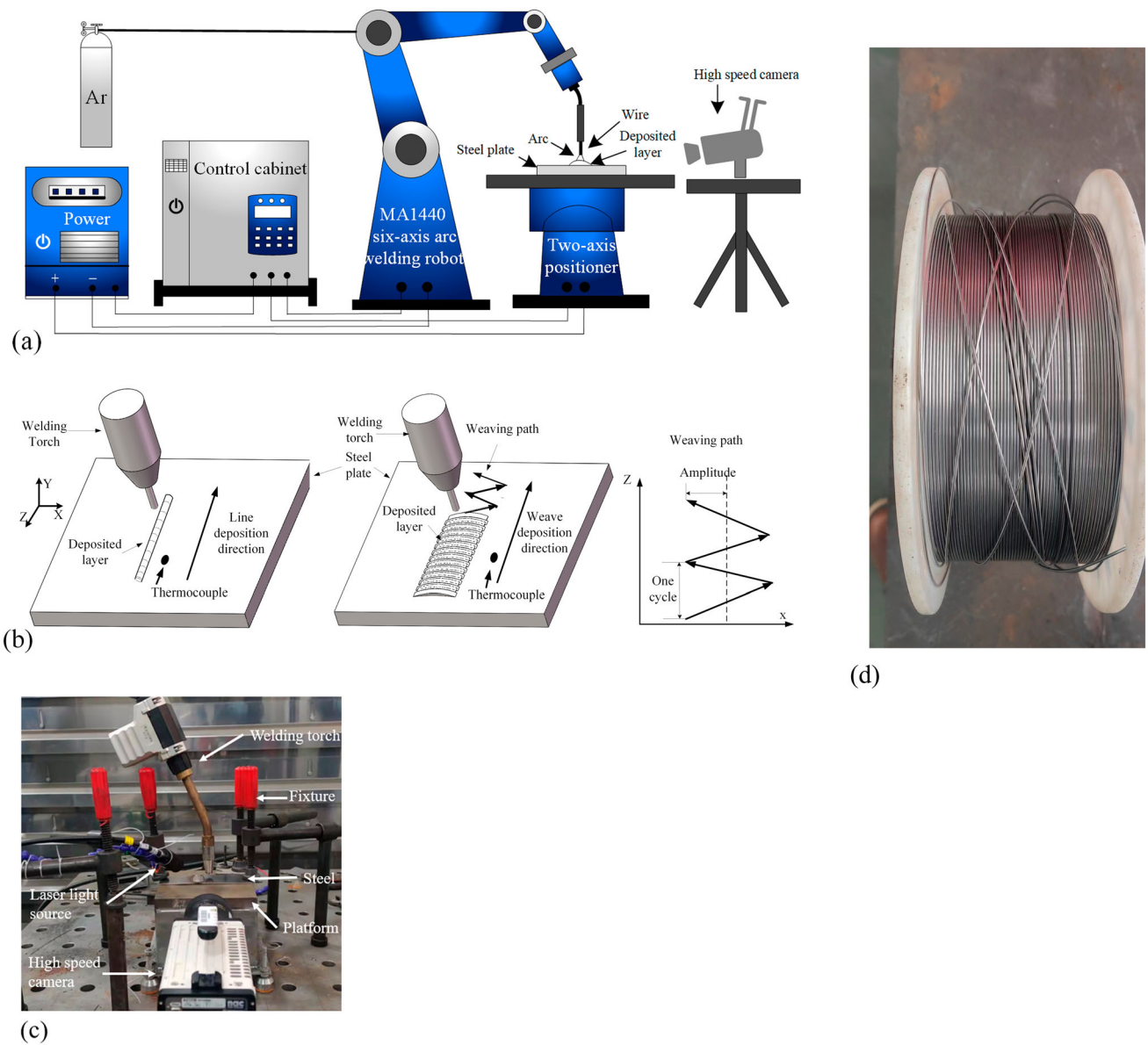
**Fig. 1** (a) Schematic diagram of experimental equipment, (b) path of both arc deposition and (c) the real setup, (d) Fe₃Al wire

**Table 1 Chemical composition (wt.%) of the experimental materials (Ref 19)**

| Materials | Fe | Al | C | Si | Mn |
|---|---|---|---|---|---|
| Fe$_3$Al wire | 85 | 17 | … | … | … |
| Steel plate | Bal | … | ≤ 0.1 | ≤ 0.05 | ≤ 0.5 |

29, 30); therefore, both the simulations picked the double ellipsoid moving heat source. In contrast to linear arc deposition, weaving heat source is constantly changing its trajectory, so its expression needs to be adjusted accordingly. A local coordinate system correlated with the moving heat source was used to determine heat flux, the specific coordinate conversion formula and the heat flux expression, and boundary condition was referred to the literature (Ref 31). The heat source model only considers the solid heat conduction equa-

tion, and the fluid flow was not considered in two cases. The convective heat transfer coefficient and thermal radiation coefficient between layer and the air were set to be unchanged. The parameters of heat input were consistent with the actual arc deposition procedure of W3 and L3. The ambient and initial temperature was set at 20 °C. The melting point of iron aluminum alloy is 1540 °C. The physical and mechanical properties of Fe$_3$Al and steel are presented in Fig. 3 (Ref 32).

## 3. Results

### 3.1 Marco Morphologies and Formability Characterization

The macroscopic morphology and cross section of the cladding obtained with the two deposition methods are depicted in Fig. 4. It can be seen that the linear arc deposition layer is relatively continuous, with sporadic oxidation and blackening

**Table 2  Process parameters used for arc deposition experiments**

| Samples | Deposition path | Current, A | Voltage, V | Deposit speed, cm/min | Amplitude, mm | Weave frequency, Hz |
|---------|-----------------|-----------|-----------|----------------------|---------------|---------------------|
| L1 | Line | 100 | 14 | 20 | … | … |
| L2 | Line | 120 | 14 | 20 | … | … |
| L3 | Line | 140 | 14 | 20 | … | … |
| W1 | Weave | 100 | 14 | 20 | 6 | 2.5 |
| W2 | Weave | 120 | 14 | 20 | 6 | 2.5 |
| W3 | Weave | 140 | 14 | 20 | 6 | 2.5 |
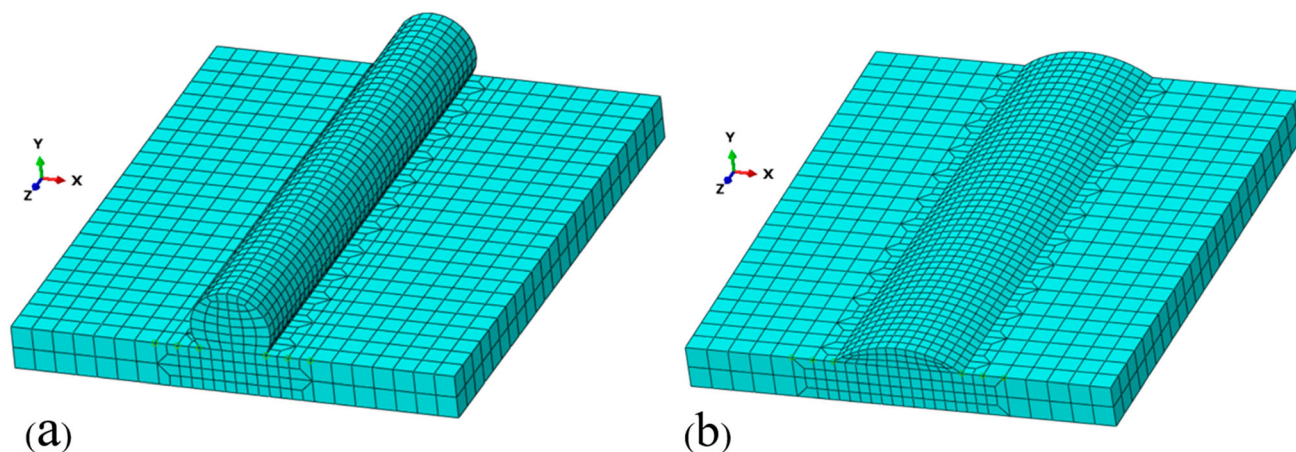


**Fig. 2**  Finite element model and meshing for arc deposition. (a) Line and (b) weave

on the surface, and higher height ($\geq$ 2.5 mm), smaller width ($\leq$ 4 mm), lower form factor and a larger contact angle ($>$ 90°) mean poor wettability with steel. As the current increases, the blackening of the surface becomes more serious, which affects the surface formability.

However, the weave arc deposition layer appears in a continuous and uniform fish-scale shape. There are no obvious defects such as lack of fusion, spatter, cracks and discontinuity. The weave arc deposition layer has a flat morphology, and lower height ($\leq$ 2 mm) and larger width ($\geq$ 10 mm), higher form factor and a smaller contact angle ($<$ 90°) indicate better wettability with the substrate. With the increase in the current, the fish-scale pattern on the surface becomes blurred, while the esthetics of the surface formability is not affected.

From the cross section, the macroscopic morphology of two arc deposition methods depicts a marked difference. The morphology of the linear arc deposition layer is close to a circle, and the contact angle is an obtuse angle, which performs poor wettability with steel. While the surface of weave arc deposition is flat with an acute angle of the contact angle, which means good wettability with substrate. In addition, the most pronounced difference is that the fusion line of the linear method is more curved, herein lies a regular pattern that the linear sample shows a significantly higher level of dilution of iron to the alloy than the weave sample.

For bimetals fabricated by arc deposition, good formability means good appearance forming without obvious defect, small contact angle and low dilution ratio. In order to accurately quantify the formability, the contact angle and dilution rate as a function of current were statistically analyzed. The schematic

diagram of the calculation of the contact angle α and the dilution rate $D$ is shown in Fig. 5(a).

The dilution ratio is mainly expressed as the dilution effect of the substrate on the deposited cladding. The dilution rate $D$ is calculated according to Eq (1) (Ref 19):

$$D = \frac{S_b}{S_a + S_b} \tag{Eq 1}$$

where $S_a$ represents the area of the $A$ area and $S_b$ represents the area of the $B$ area. Each area was measured and calculated in ImageJ software.

For two diverse deposition methods, the contact angle and dilution rate under different currents are given in Fig. 5(b).

The wettability is characterized by the size of the contact angle. Figure 5(b) shows that as the current increases, the contact angle gradually increases, and the deposition cladding obtained with the weave deposition method has a better contact relationship with the substrate than the deposition layer obtained with the line arc deposition method. Furthermore, it is worth noting that under the same current, the value of dilution rate of weave arc deposition is significantly lower than that of linear arc deposition, which means that during linear arc deposition, more steels have metallurgical reactions with liquid alloy, and this may be one of the reasons for the variance in formability, as for the cause of the low dilution rate and small contact angle of the weaving process, it is discussed in Sect. 4.1. Combined with the macroscopic morphology and these data, it can be concluded that the obtained formability of the weave deposition methods is superior to linear deposition methods.
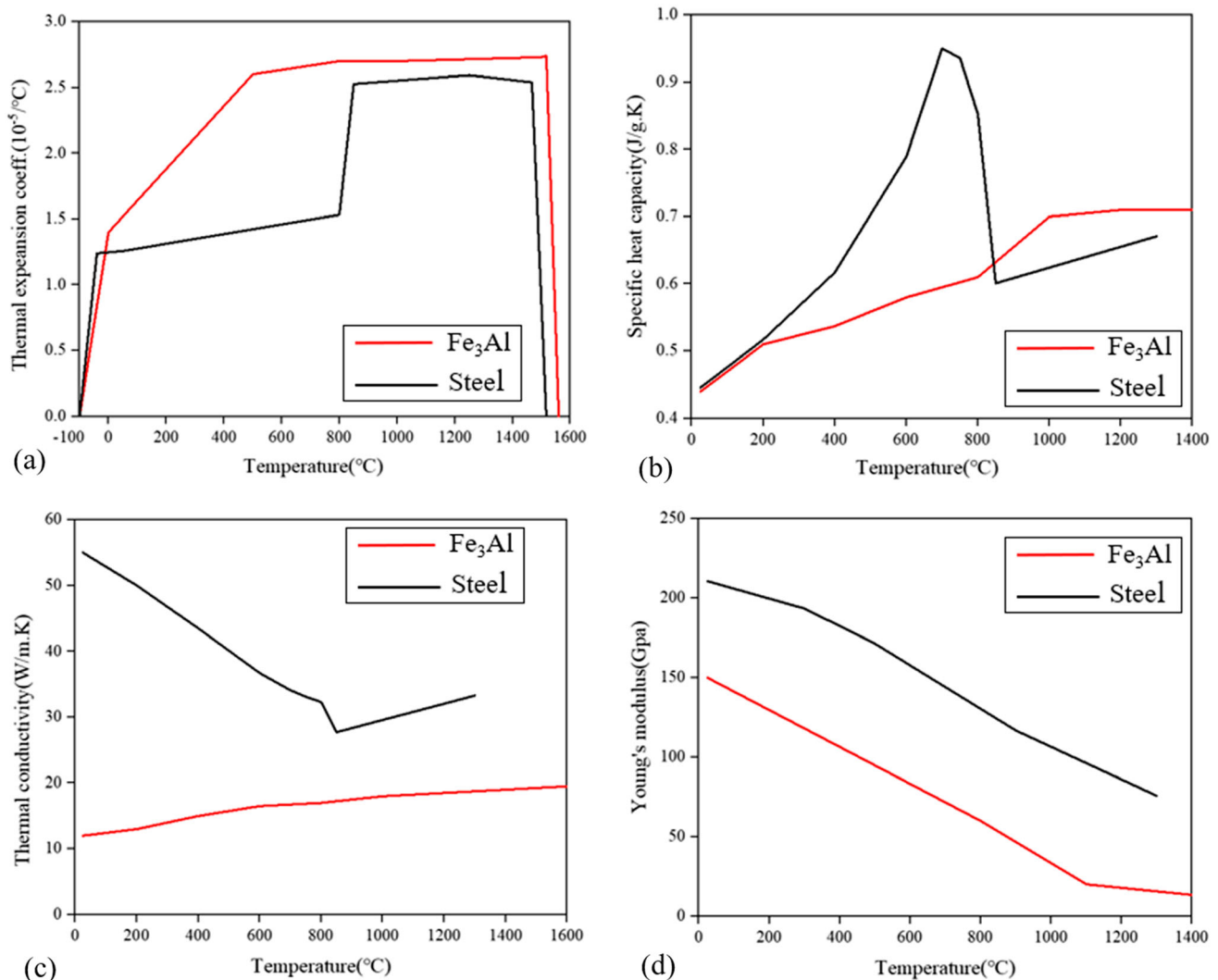
**Fig. 3** Physical and mechanical properties of Fe₃Al and steel. (a) Thermal expansion coefficient, (b) specific heat capacity, (c) thermal conductivity and (d) Young's modulus
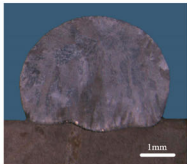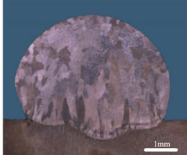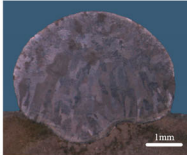
### 3.2 Micro-Morphologies and Phase Composition Characterization

The metallographic morphology of the linear arc deposition layer is shown in Fig. 6(a) to (d). The metallographic diagram performs various light and dark grains, owing to the fact that such grains exhibit various crystal growth orientations. Two diverse microstructures were observed in the deposited cladding: Equiaxed grains on the top and columnar crystals grow from the interface to the middle and upper region. The growth direction of the columnar crystals is not perpendicular to the substrate, but perpendicular to the fusion line. Similar to the linear arc deposition morphology, the metallographic morphology of the weave arc deposition in Fig. 6(e) to (h) involves distinct light and dark grains, and microstructures ranging from equiaxed grains on the top of the layer to columnar crystals in the inner and bottom region. The majority of columnar crystals are nearly perpendicular to the steel substrate, meaning that the maximum heat is dissipated in this orientation. The deposition layers, in both cases, exhibit the characteristics of a rapid solidification structure and the grain morphology transformation from columnar crystal to equiaxed crystal.

For a more accurate comparison, the diameters of the columnar grains in width and the equiaxed grains were counted, and a fitting distribution trend curve of grains size distribution map was derived based on the statistics. Figure 6(i) and (j) evidently shows that the grain size of the linear way is significantly larger than that of the weaving way, suggesting that the linear way grain has grown during solidification. This issue will be addressed in 4.2 with regard to the factors affecting grain growth with the experimental and simulation results.

Figure 7(a) and (b) demonstrates the presence of a transition region near the fusion line, where the iron and aluminum content changes dramatically, and the width of this transition region varies by roughly 40 μm for the linear sample and 20 μm for the weaving sample. Moreover, the weave sample has a relatively smooth interface; the aluminum element is evenly distributed without segregation, which indicates that the composition of cladding is relatively single.
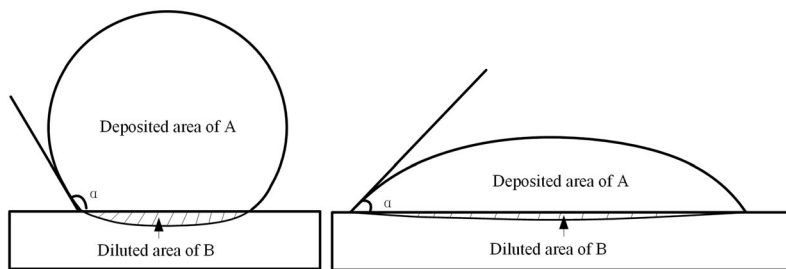
**Fig. 4** Macroscopic morphologies and cross-sectional images of the cladding. (a) Line and (b) weave
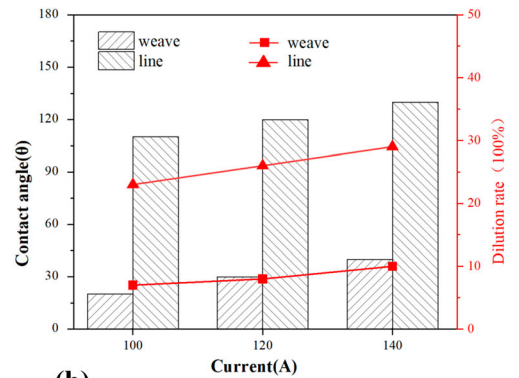


**Fig. 5** (a) Schematic diagram of contact angle $\alpha$ and dilution rate D and (b) $\alpha$ and D under different currents
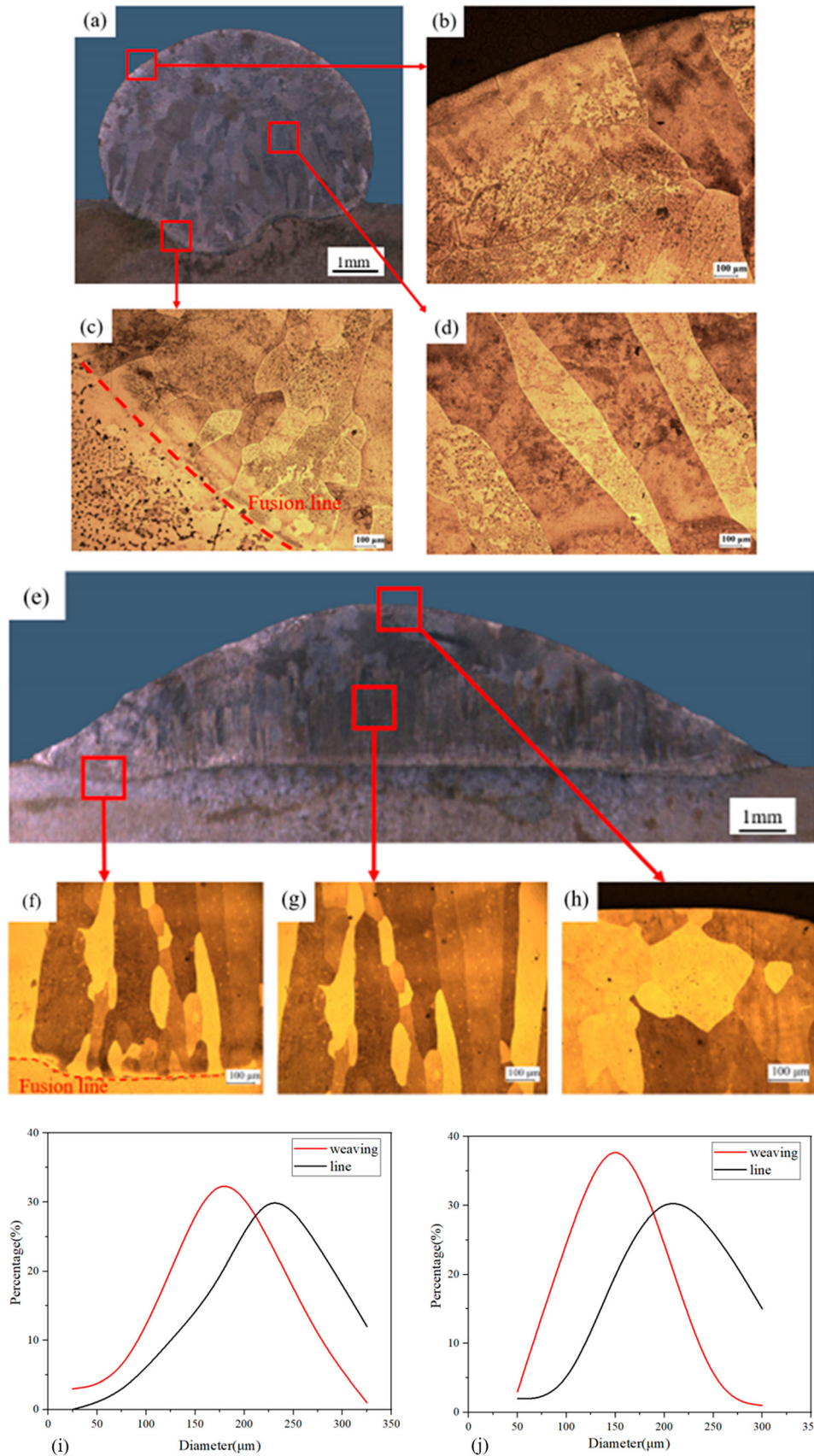
**Fig. 6** Microstructures of the Fe₃Al cladding: (a) metallographic microstructure of linear way, (b) equiaxed grains at the top in line, (c) fusion line at the interface in line, (d) columnar grains in the interior in line, (e) metallographic microstructure of weave way, (f) fusion line at the interface in weaving, (g) columnar grains in the interior in weaving, (h) equiaxed grains near the interface in weaving, (i) fitting distribution trend curve of columnar grains size distribution map in the width direction, (j) fitting distribution trend curve of equiaxed grains size distribution map

On the SEM images and EDS of the W3-deposited layer of Fig. 8(a) and (b), it can be seen that Al content was 15.6 wt.%, which was within Fe₃Al's range. The element C was introduced from the molten iron sheet of wire. Therefore, this evidence can prove the accuracy of the Fe₃Al flux-cored wire. What is more, the grains were staggered and different in light and dark, and this was due to the different orientations and corrosion degrees of these grains. There was no difference in the element composition of grains with different light and dark based on the Fe and Al concentration distribution diagram of the deposition layer.

Figure 8(e) shows that the deposition layers of six samples are primarily composed of FeAl and Fe₃Al phases. The oxide phase, Fe phase and Al phase were not detected. According to the Fe-Al binary phase diagram (Ref 19), when the molten Fe₃Al alloy (Al content was close to 16%) cools slowly from high temperature, it changes to the partially ordered B2-FeAl phase; then, at the ordering temperature, B2-FeAl phase transforms into the fully ordered DO₃-Fe₃Al phase. However, this transformation needs to be maintained at the critical temperature for a long time to realize the redistribution of Fe and Al atoms. Due to the rapid cooling rate during the arc deposition, the ordering process cannot be fully carried out; thus, a large fraction of FeAl phase with B2 structure will remain in the deposited layer. Therefore, FeAl and Fe₃Al phases were detected in the XRD diffraction patterns.

In order to clarify the generated phases, the deposited layer of W3 was characterized by TEM, and the results are shown in Fig. 8(f). TEM morphology showed obvious dislocation entanglement and an electron diffraction pattern of B2-FeAl phase along [001] axis. Therefore, combined with XRD and TEM characterization, the phase formed is mainly B2-FeAl phase rather than other phases.

### 3.3 Hardness and Bonding Strength

Figure 9 shows the hardness distribution diagram of the cross section of L3 and W3. There is a clear difference in hardness between the deposited layer and the substrate. The hardness of the cladding layers ranges from 314 to 345 HV and that of steel ranges from 115 to 134 HV, and there are no obvious transition layers between the two layers. The hardness of both deposited alloys is not affected by the various deposition processes, and it is the same phase formed during arc deposition that accounts for the same hardness of the Fe₃Al-deposited alloys. Furthermore, both diagrams show a region with significantly greater hardness at negative distances from the steel. This suggests that more Fe₃Al alloy has been deposited and diffused into the steel substrate, increasing its hardness. The dilution area of the line is larger than that of the weave, which is consistent with the dilution ratio shown in Fig. 5.

The bonding strength of deposited alloys and steel was tested according to the destructive testing method of the bimetallic bonding strength which referred to the national standard GB/T12948-1991. According to the regulations, the tensile speed was controlled by means of stress, and the applied velocity was 1 mm/min. The schematic and image of the specimen are displayed in Fig. 10(a) and (b). Figure 10(c) shows the principle of the test for bonding strength between the deposited layers and steel substrate. The bonding strength was calculated according to the following formula:

$$\sigma = \frac{F_{\max}}{A} \tag{Eq 2}$$

where $F_{\max}$ is the compressive force and $A$ is the area of the interface between the deposited layer and steel substrate.

Figure 10(d) illustrates the variation in bonding strength for samples under six diverse samples. There exists a considerable difference between the bonding strength of weave and line method, L1 is 48.86 MPa while W1 is 123.69 MPa; with a significant increment of 153.15% in bonding strength, these collected data prove that arc deposition with weaving has an obvious advantage in fabricating bimetal samples with higher bonding strength. In addition, it is noteworthy that the bonding strength of the two processes gradually decreases as the current increases; specifically, L3 has a 30.9% lower strength than L1, while W3 is 12.6% less than W1.

Figure 10(e) and (f) shows obvious river patterns and large cleavage steps in the fracture morphology of Fe₃Al alloy; this evidence suggests that the fracture site is located in the deposited layers near interface instead of the steel substrate. Fe₃Al alloy, regardless of whether formed in weaving or line path, is prone to cause a brittle fracture when measuring the bonding strength. So in this regard, the forming path is not a factor affecting the fracture mode of the bimetallic failure, as the influence of two paths and current on bonding strength will be discussed later in Sect. 4.3.

## 4. Discussion

### 4.1 Dynamic Behavior of Molten Pool

In industrial production, welding with weaving has been used widely to obtain better weld quality by avoiding lack of side wall fusion and improving the weld efficiency by obtaining the wide weld bead (Ref 33). There is a lack of understanding about the effect of weave on the formability of the weaving, and very few studies have investigated molten pool morphology in the arc deposition process. Hence, clearer molten pool morphologies were obtained by applying a high-speed camera. Figure 11 displays the deposition layers and the molten pool morphology of two methods.

It is noted in better detail that the molten pool differs in size, but not in shape. The size of the molten pool of linear deposition is much larger than that of the weaving method. The shape of the molten pool has been marked with red boundary lines. Along the direction of the torch, it presents a double ellipsoid shape, in which the semi-axis of the anterior ellipsoid is shorter than that of the posterior ellipsoid. The shape of the two molten pools is similar to the typical shape of the molten pool illustrated in Fig. 11(a). In the course of arc deposition, the wire is heated by the arc and melts rapidly and then falls into the molten pool, while the molten pool moves with the torch's regular movement.

The distinction between two means is mainly due to the contrasting velocity of molten pool. Based on the above diagram, the model of the melt pool is simplified, and the schematic diagram of velocity models for linear and weaving molten pool is presented in Fig. 12(b) and (c). Compared to the linear arc deposition with only one direction of velocity, the weave arc velocity involves two perpendicular sub-velocities,
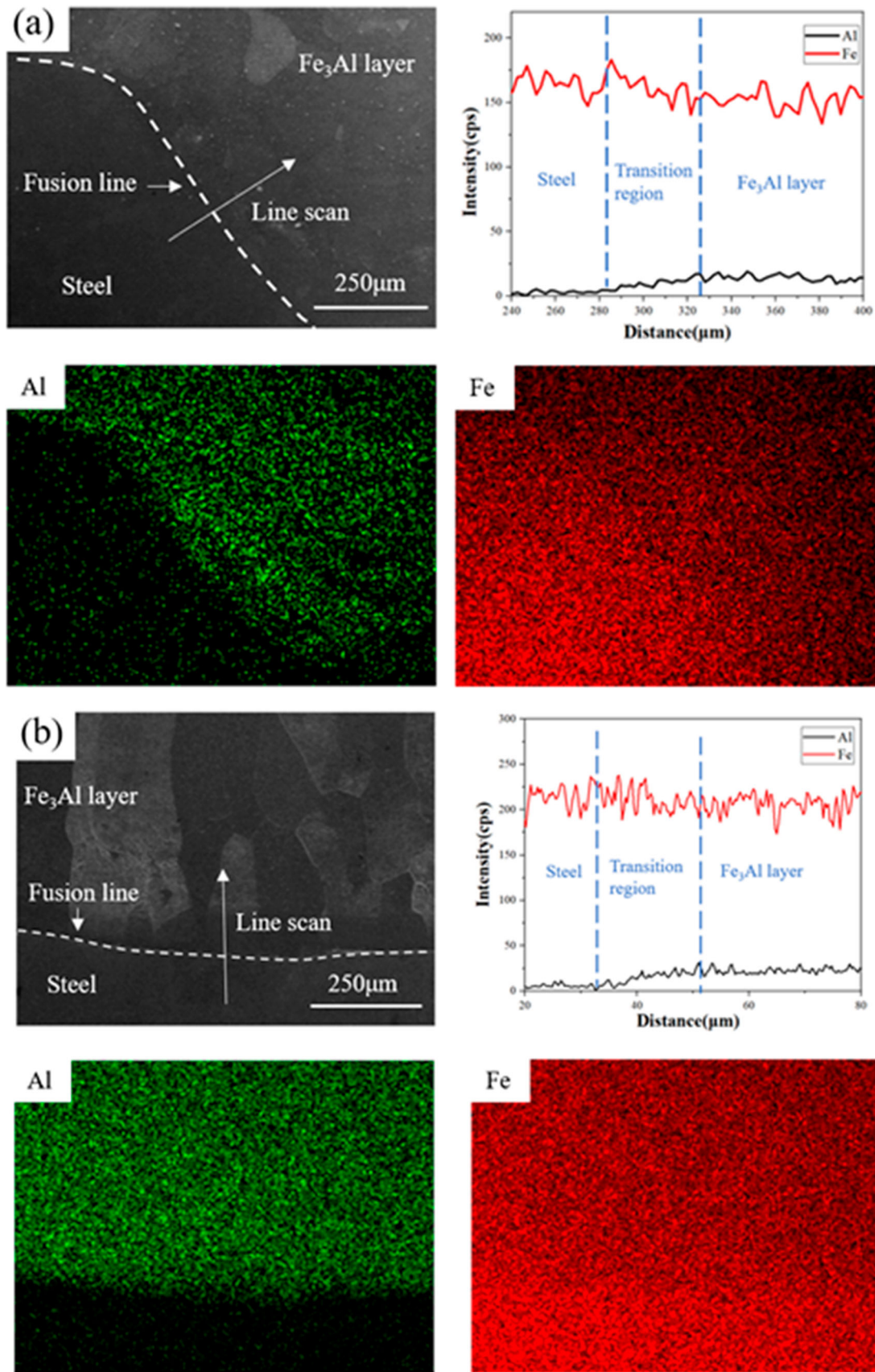
**Fig. 7** (a) SEM images of the line scan and area scan by SEM in line and (b) SEM images of the line scan and area scan by SEM in weaving
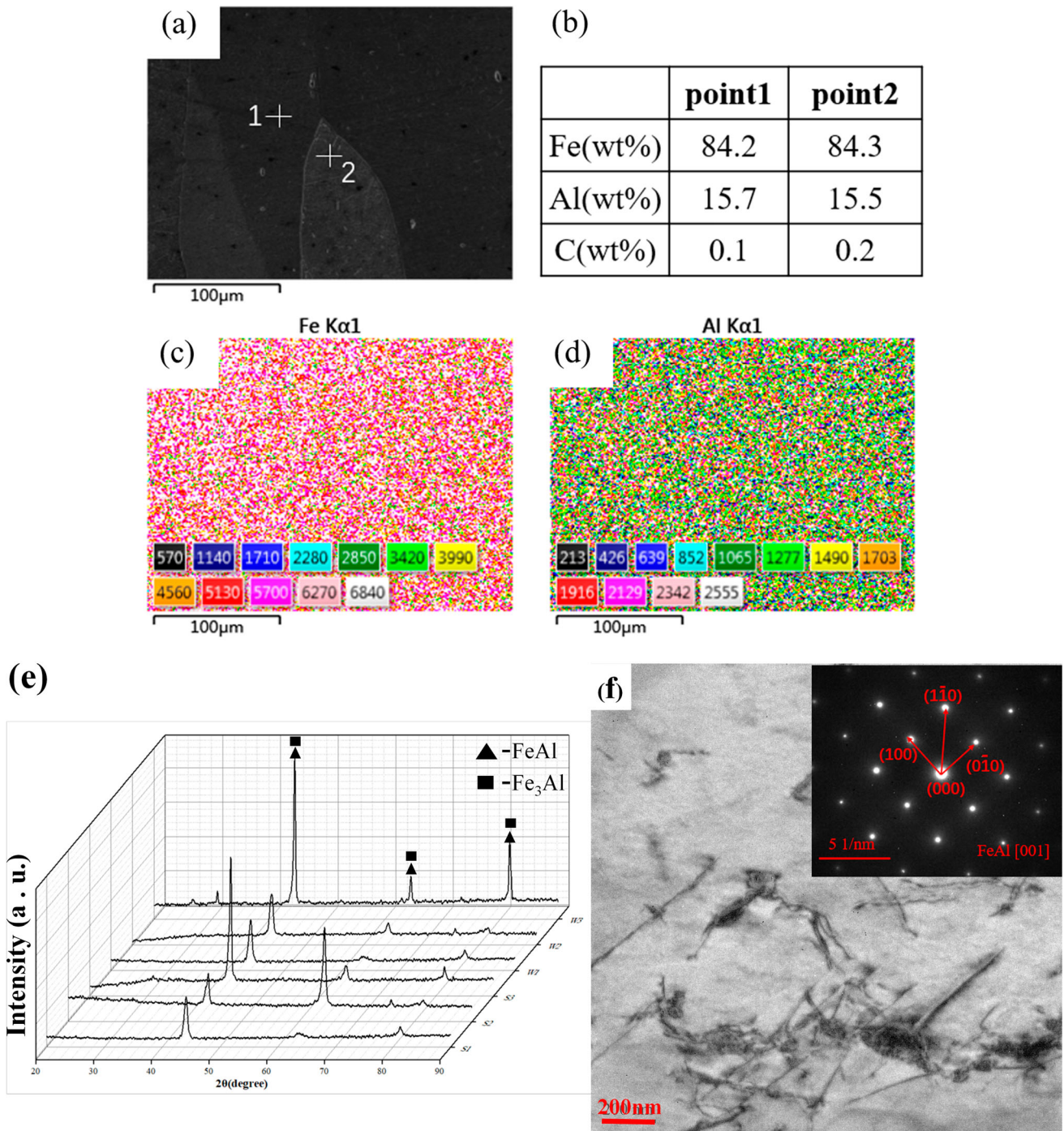
**Fig. 8** (a) SEM morphology, (b) point composition, (c) Fe concentration distribution diagram, (d) Al concentration distribution diagram, (e) XRD diffraction patterns of the deposited layers, (f) TEM micro-area morphology and selected area diffraction spots

namely the molten pool velocity along the deposition direction and a lateral velocity perpendicular to the deposition direction.

The total velocity $v$ of the weave arc molten pool can be expressed as follows (Ref 34):

$$w = 4lf \tag{Eq 3}$$

$$\theta = \arctan\frac{u}{w} = \arctan\frac{u}{4lf} \tag{Eq 4}$$

$$v = \sqrt{u^2 + w^2} = \sqrt{u^2 + (4lf)^2} \tag{Eq 5}$$

where $u$ is the velocity in the deposited direction, $w$ is the lateral velocity, $f$ is the weave frequency, $\theta$ is the angle between $v$ and $w$, and $l$ is the weave amplitude.

Equation (2) shows that the larger the weave amplitude and frequency, the smaller the $\theta$. The calculation demonstrates that during the arc deposition, the lateral velocity $w$ is much greater than the deposited direction velocity $u$. Equation (5) indicates that
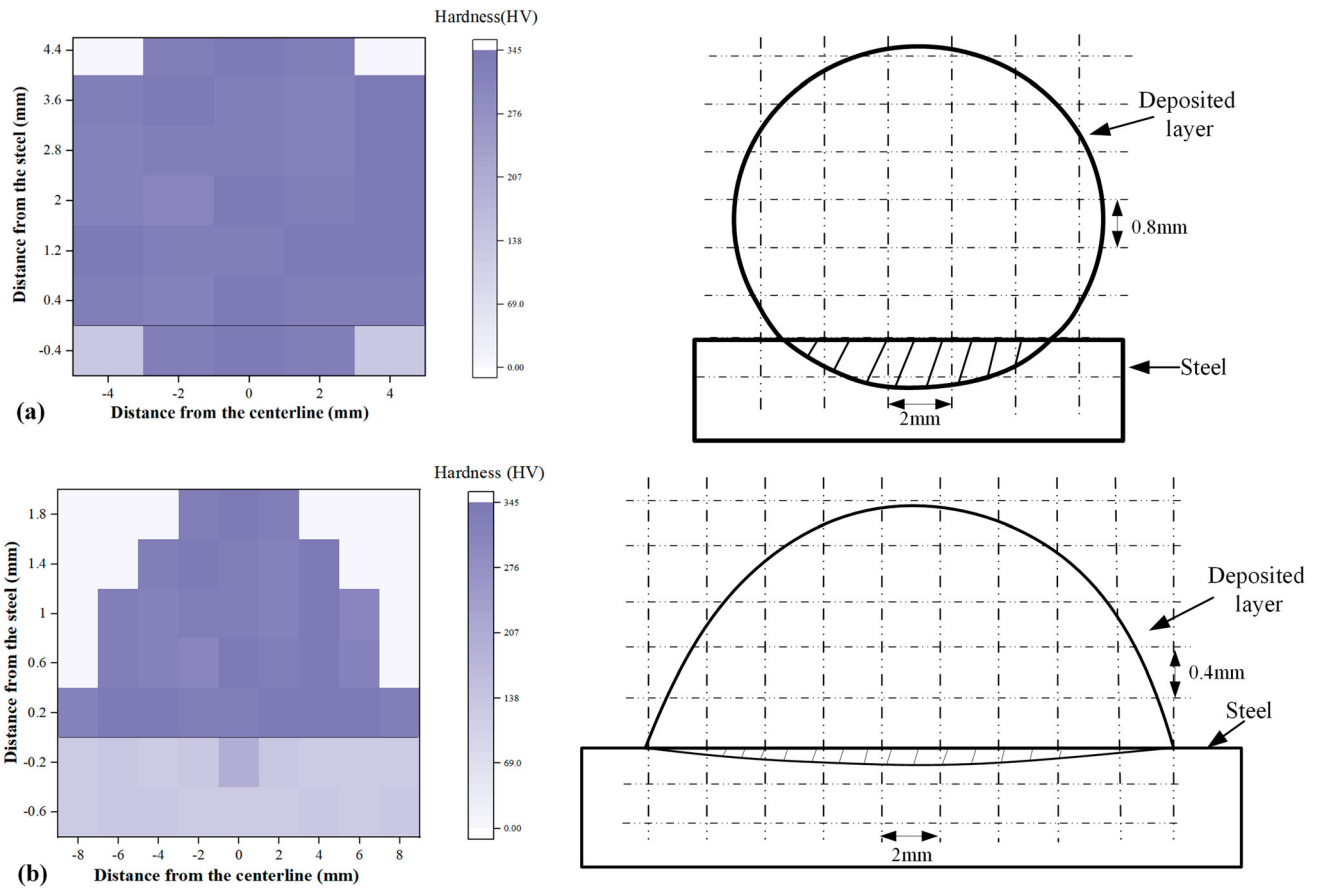
**Fig. 9** Hardness distribution diagram and the coordinates to the measuring location on the cross section of (a) line and (b) weave

that the weave arc molten pool velocity $v$ is 0.06 m/s, which is much greater than the linear molten pool velocity $u$ of 0.0033 m/s.

A major factor in determining the size of molten pools is the velocity, which is responsible for a substantial amount of the volume of pool. Alternatively, when the current and voltage are constant, the width of the molten pool $B_{max}$ and the penetration depth $H_{max}$ are approximately linearly reduced simultaneously with the increase in the velocity, thereby reducing the volume of the molten pool. Taking into account that the weaving velocity $v$ is much greater than the linear velocity $u$, this causes the molten pool to be smaller in both width and penetration depth, which is what causes the dramatic contrast between the dimensions of the molten pool in Fig. 11.

In regard to Fig. 12(d) and (e), the schematic diagram presents a schematic summary of the metallurgical reaction of a molten pool of steel in proportion to the size of the molten pool. Due to the fact that the molten pools of different sizes differ in volume, the dilution rate will differ significantly. In linear arc deposition, the contact angle is primarily determined by the balance among the surface tension of the molten pool, the gravity and the arc force. It is believed that the whole liquid molten pool, at this point, is in a relatively stable state, and the size of the contact angle depends primarily on the wettability of the material and the substrate. Since the wettability between liquid $Fe_3Al$ and the steel is very poor, the solidified layer will maintain this poor wetting relationship along the torch direction

at all times during linear method. Due to this reason, the contact angle is very large as shown in Fig. 4(a).

During weaving deposition, the alloy is deposited on a substrate with a large area of contact, which permits it to spread to a considerable extent, thereby resulting in a small contact angle. Moreover, there are other factors in the perspective of fluid that are also conducive to the formation of small contact angles, which have not been discovered and investigated in previous studies. The molten pool in weave arc deposition, moving with the periodic lateral movement of the torch, is in a state of instability. Since its volume is smaller than that of line case, the arc force has played a leading role on the fluidity and spreading of the molten pool, which is considered the principal determinant of its contact angle.

As shown in Fig. 13(a), the end of the wire is not straight but inclined to the right for a certain angle, as the torch is about to move toward the right boundary. This happens when the weaving torch advances rapidly, arcing and burning of the wire will be preferentially along the forward direction, with continued forward movement, the end of the wire will form an inclined plane. It is the uneven wire end, in this way, which causes the arc force to alter from being perpendicular to the molten pool to being inclined to the molten pool at the same angle, thereby the arc force can be decomposed into vertical and horizontal components. The arc force mainly affects the deformation of the molten pool surface, during arc deposition process, molten metal is subjected to arc force, and the schematic diagram of arc force is provided in Fig. 13(b). Some
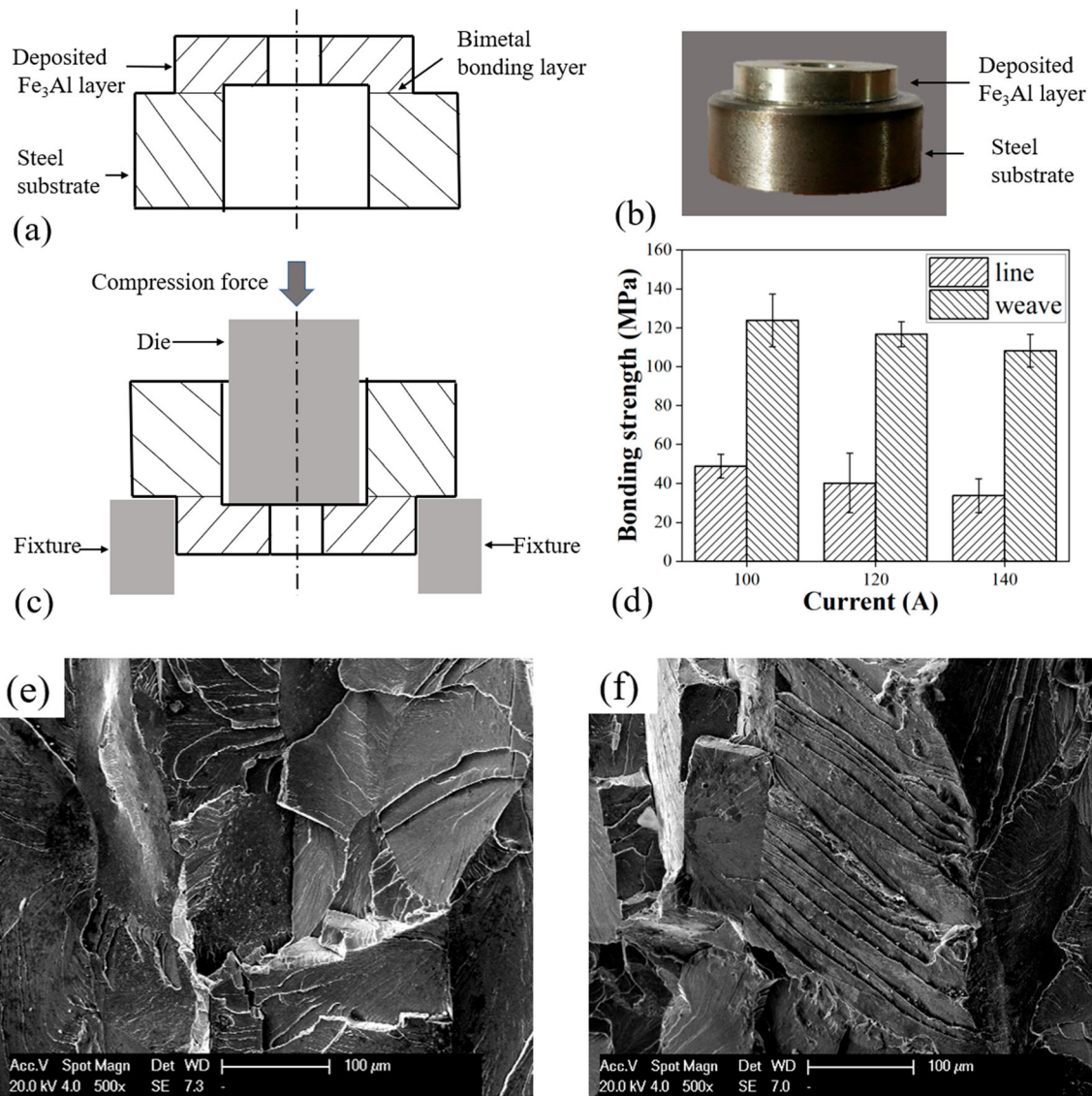
**Fig. 10** (a) Schematic of test specimen, (b) sample for the test of bonding strength, (c) principle of the test for the bonding strength, (d) the bonding strength of six samples between $Fe_3Al$ alloys and steel substrate, (e) fracture morphology of L1 and (f) fracture morphology of W1



**Fig. 11** Molten pool morphologies of two approaches: (a) line and (b) weave
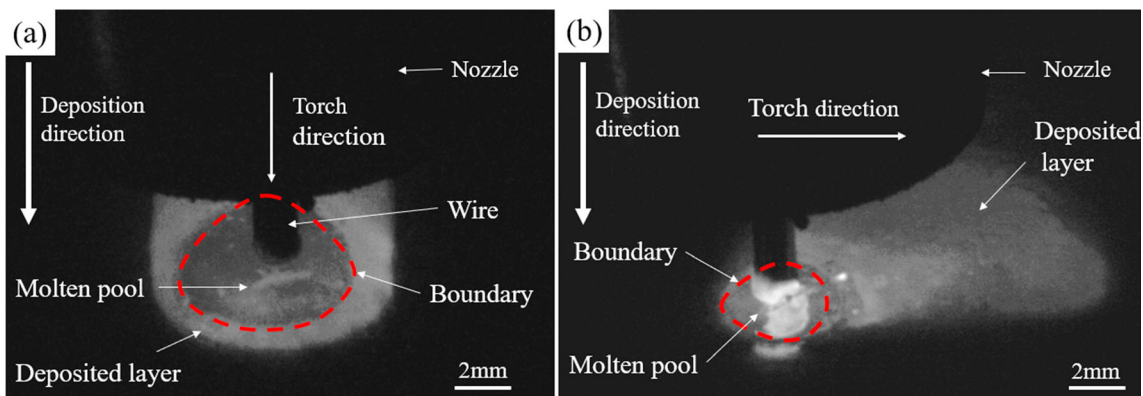
liquid metals are driven to the boundary of the molten pool at high speed due to the existence of horizontal components, which favors the deformation of the molten pool surface and a relatively smaller contact angle at the boundary. So it can be concluded that weave arc deposition has a better spreading cladding and a small contact angle with the substrate.
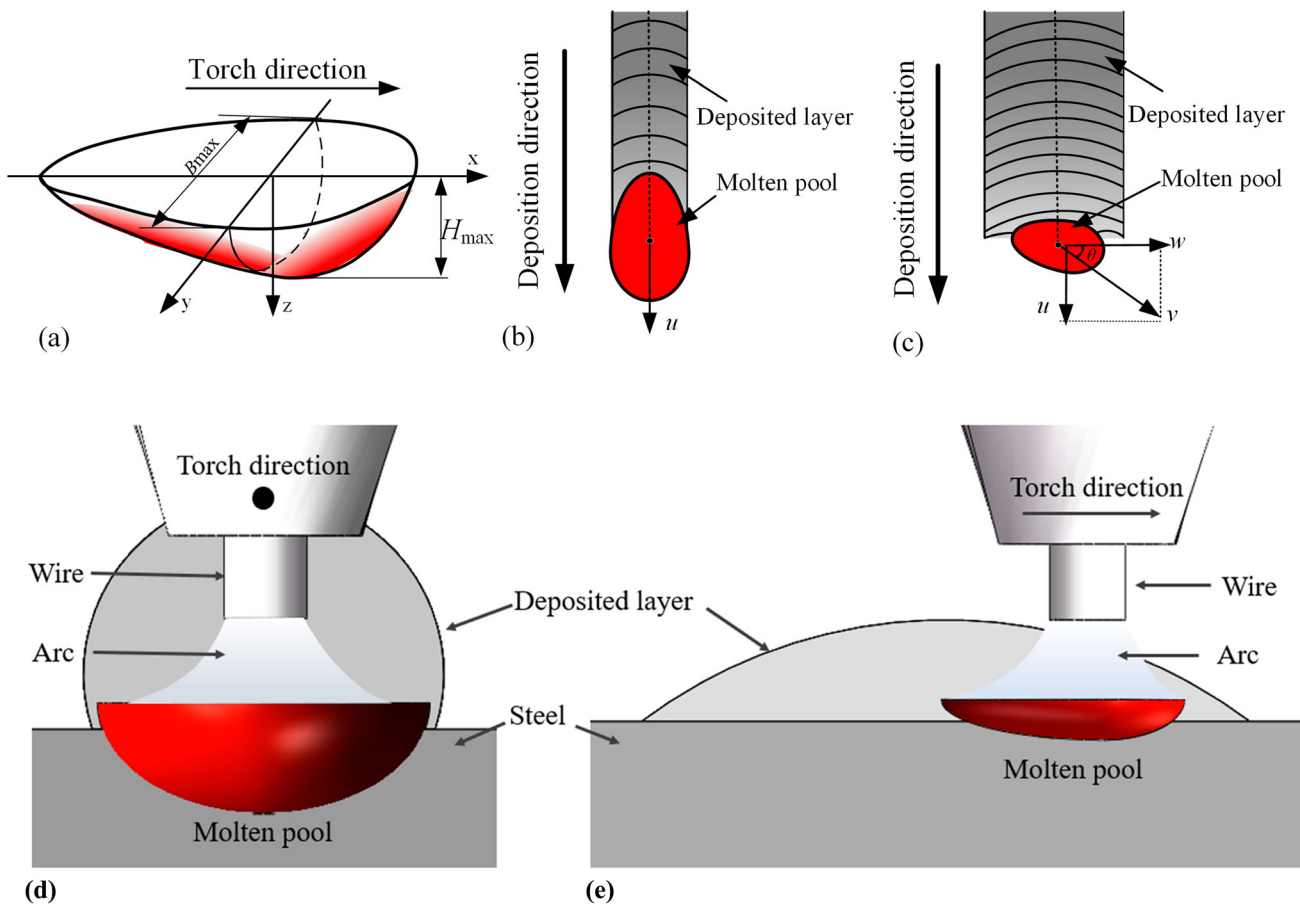
**Fig. 12** (a) Schematic diagrams of the shape of the molten pool (Ref 34), (b) velocity models in linear way, (c) velocity models in weaving way, (d) schematic of cross section of molten pool in linear way and (e) schematic of cross section of molten pool of weave way
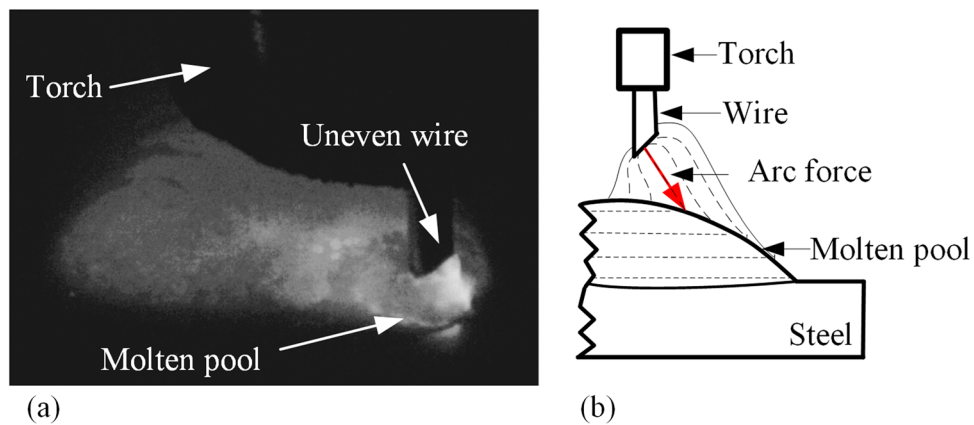


**Fig. 13** (a) Image of the molten pool moving to the right boundary and (b) schematic diagram of arc force

### 4.2 Finite Element Simulation Characterization

The simulated temperature distribution along the path of arc deposition at the same time is provided in Fig. 14. A comparison of two methods reveals a clear distinction. As shown intuitively in Fig. 14(a), there is a regular large elliptical pattern in linear process, and a symmetrically distributed temperature field of a cross section is obtained from the simulation in Fig. 14(d), which is in general agreement with the experimental results in Fig. 4(a). As the boundary of the peak

temperature in linear arc procedure is elliptical, it indicates that the heat is mainly concentrated in the center of the cladding and radiates around this peak temperature region. Figure 14(b) shows the first half cycle of the arc moving from the left to the right, there is a clearly visible oval shape to the molten pool as a whole, and the high-temperature area is elongated to the right. Similarly, as the arc moves from right to left in the second half cycle of Fig. 14(c), the high-temperature area of the molten pool expands to the left. For the entire line simulation, the temperature field's shape remains nearly constant, whereas for
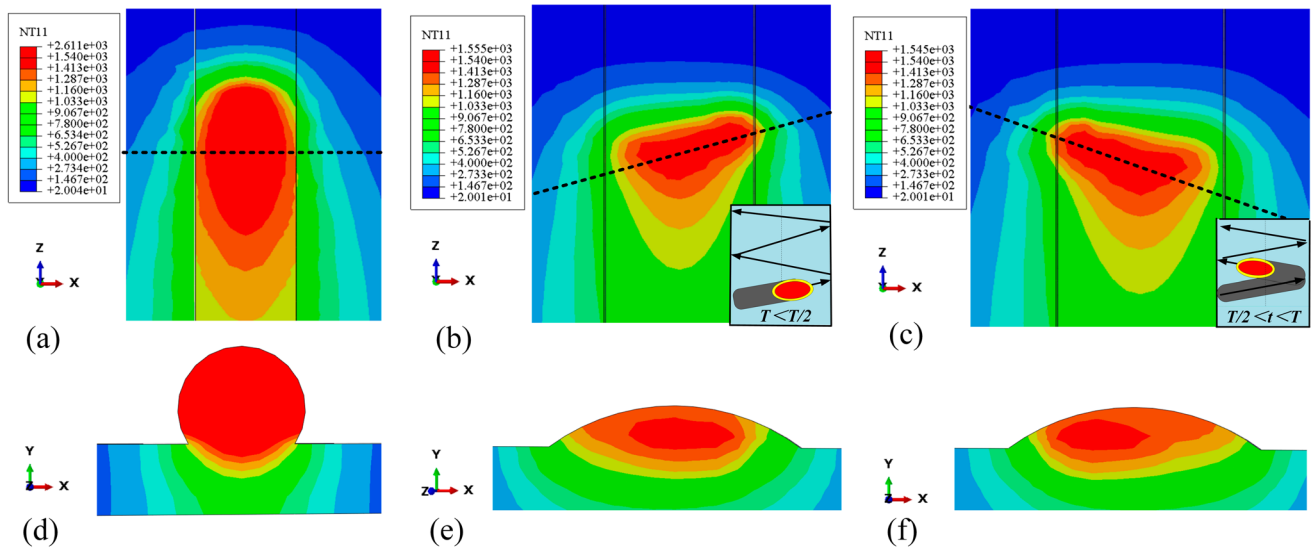
**Fig. 14** Simulated temperature field (a) in linear process, (b) in the first half of the weave process, (c) in the second half of the weave process, and cross section of simulated temperature field (d) in linear process, (e) in the first half of the weave process and (f) in the second half of the weave process

the weaving case, it is totally different, since the shape of the temperature field continues to change throughout the whole process.

An evident molten pool shows a narrow ellipse shape in the cross section along the forward direction as given in Fig. 14(e) and (f), considering that the area of the high-temperature molten pool is much smaller than the area of the linear deposition. Moreover, the boundary of weave operation is almost as straight as the substrate, demonstrating explicit directionality of maximum heat dissipation perpendicular to the substrate. Meanwhile, there is no evidence of heat accumulation in the middle, proving that the heat is evenly spread over a larger area of the substrate; it is probably due to the way in which the high-speed movement of the torch stirs the molten pool and promotes the flow of the melt, eliminating the overheating at the center of the deposited layer and making the temperature distribution throughout the cladding more uniform.

For the purpose of quantifying the change of the temperature field, thermal cycles were calculated and measured for each case. According to Fig. 15(a), four thermal cycle curves all exhibit a sharp increase at first and then followed by a gradual decline; it seems that the overall trend of the experimental temperature is approximately in line with the calculated temperature, which reveals the FEA simulation is closely related to the actual deposition operation. Additionally, it has been found the peak temperature of the line arc deposition is higher than that of the weave arc deposition regardless of whether data was returned from experiments or simulations. This is due to the weaving velocity being high, the linear energy and heat flux density being low, as well as the heat flux distribution area being large, which means the heat input per unit area is rather low, the energy is dispersed, and the peak temperature is relatively low.

The thermal cycle curves of two nodes are also collected at the corresponding regions of grain morphology within the deposited layers of the two cases, so as to quantify the difference in temperature change during solidification. Significantly, the calculated thermal cycles of weave method fluctuate drastically several times before reaching the peak temperature.

It is the periodical movement of the molten pool approach to and away from the calculated point, which causes multiple fluctuations in the curve.

In both processes, the thermal cycle curves rise to the peak temperature, and the falling temperature tends to be the same when cooling. Most notably, due to the fact that the slope of the weave curve drop is greater than that of the linear curve, the cooling rate of weave method is greater than that of line way. Two key factors needed to be accounted for this pattern: One is the weaving torch acts as a stirrer for the molten pool, which contributes to cladding cooling during solidification; and the other is that the weave deposition layer with a larger bonding area is conducive to faster heat dissipation. The discrepancy of grain size in varied regions between two deposition methods is attributed to the variance in cooling rate; the faster the cooling rate, the finer the grain size, which is main factor that causes the grain size of the weaving way is significantly finer than that of the linear way as presented in Fig. 6(i) and (j).

The temperature distribution affects the solidification behavior of metal. Two key factors are temperature gradient $G$ and crystallization rate $R$ (Ref 34). The influence law of these two factors on microstructure morphology and size is shown in Fig. 15(c). The larger the cooling rate ($G \times R$), the smaller the microstructure size. On the other hand, the morphology parameter ($G/R$) affects the morphology of microstructure. With the decrease in parameters, the morphology of microstructure changes from equiaxed crystal to cellular crystal, columnar crystal and equiaxed crystal.

The formula of R can be expressed as follows (Ref 34):

$$R = V \cos \theta \qquad \text{(Eq 6)}$$

where $V$ represents the total velocity of molten pool and $\theta$ represents the angle between the forward direction of molten pool and the normal direction of this point.

According to the thermal cycle curves and formula of $R$, calculation of the $G$ and $R$ of various nodes in two deposited layers of different morphologies are shown in Fig. 15(d). There are some similarities to be found between the two processes.
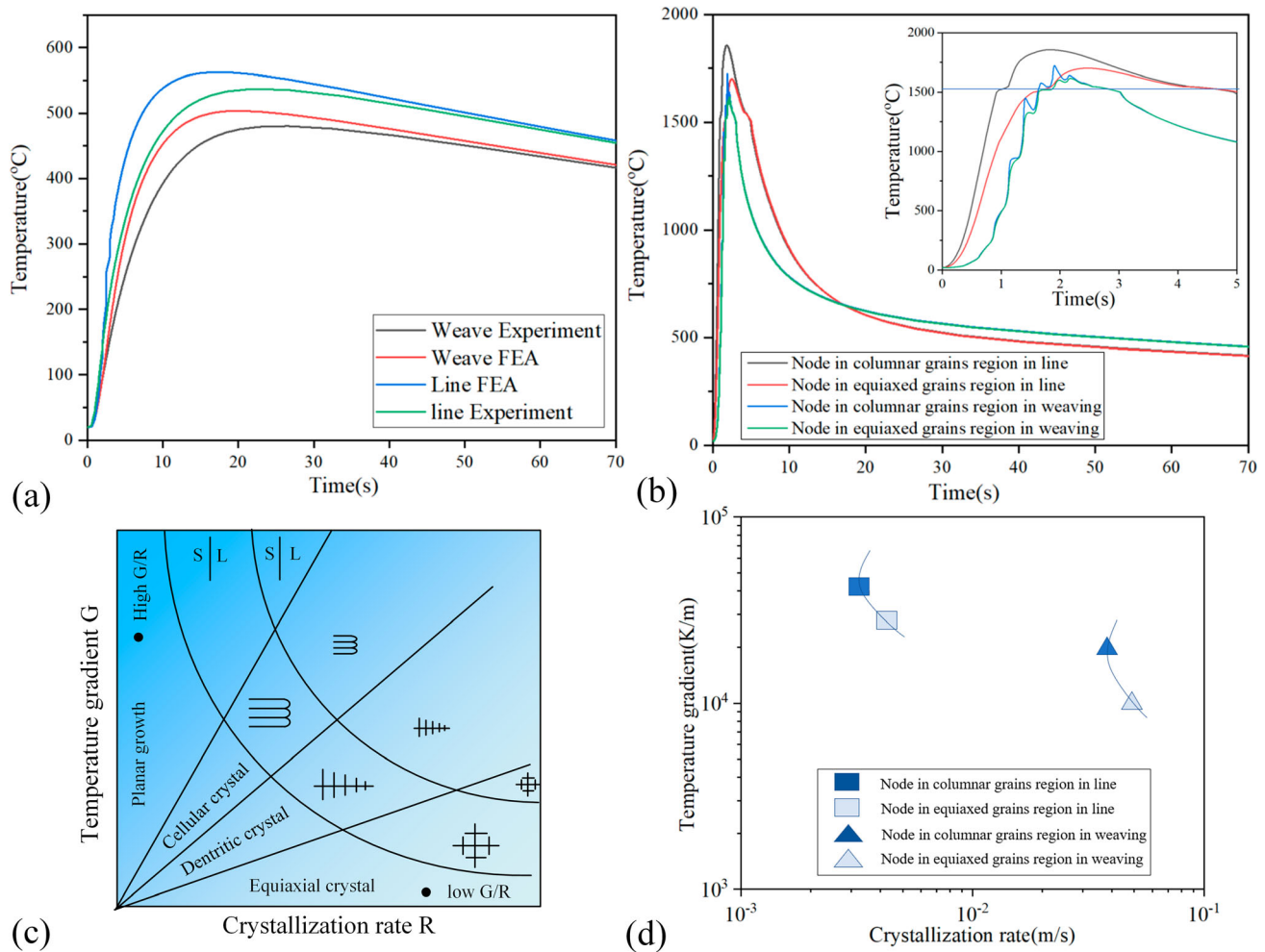
**Fig. 15** (a) Thermal cycle curves of the calculated and measured points of the two processes, (b) thermal cycle curves of different nodes, (c) formation mechanism of solidification structure (Ref 34) and (d) calculation of the G and R of various nodes

The $R$ of the equiaxed crystal region is significantly faster than that of columnar crystal region. The key reason is that $\alpha$ is smallest in the upper equiaxed crystal region, resulting in $R$ being the fastest, whereas in the lower columnar crystal region, $\theta$ is close to vertical; thus, $R$ is the slowest. Additionally, there is a tendency that $G$ increases from the upper equiaxed crystal to the lower columnar crystal, mainly because the lower region is located near the substrate and away from the heat source, which results in a sharp change of temperature when cooling.

For the above-mentioned reason, similar solidification processes occur during both processes. At the beginning of the solidification, the molten alloy cools rapidly and nucleates at the solid–liquid interface. As solidification progresses from the interface to the center of the deposited layer, the grains present a columnar crystal morphology in virtue of high $G/R$. When solidification is close to the surface of the deposited layer, $G$ decreases along with $R$ increasing, and it is easier to form equiaxed crystal morphology with low $G/R$. These mechanisms are basically a major contributor to similar microstructure of two processes as described in Fig. 6.

In the region with similar morphology, the key parameters $G$ and $R$ are totally different between the two processes. Owing to the velocity of weave arc molten pool being greater than that of the linear method, the $R$ in weaving is also much greater than

that in line. Meanwhile, since the molten pool is smaller during weave arc deposition, heat concentration is reduced and the maximum temperature is lower, resulting in a lower $G$ during cooling than linear deposition. Furthermore, columnar to equiaxed transition occurred during solidification in both processes, but the transition threshold is disparate. In conclusion, it has been shown that arc deposition processes involving contrasting paths result in various temperature field distributions, which determine varied solidification parameters $G$ and $R$ in different regions, and eventually lead to distinct solidification microstructure morphologies and grain sizes.

### 4.3 Microstructure and Residual Stress at Interface on Bonding Strength

Since the fracture sites mainly take place at the Fe₃Al alloy-deposited layer near the interface, the microstructure and the residual stress at the interface both have a considerable impact on the bonding strength, the improvement of bimetallic bonding strength by weave process can be explained by these two aspects.

The microstructure at the interface is shown in Fig. 16(a) and (b). In both samples, fine grains and columnar crystals distribute along the fusion line. It is observed that the average diameter of fine grains in the linear sample is 230 $\mu$m, as well

as the columnar crystal width is 300 $\mu$m, while corresponding weave samples are 90 $\mu$m and 110 $\mu$m, indicating that the microstructure at the interface of weave layer is refined.

For Fe$_3$Al alloy, the fracture stress is strongly correlated with grain size. The cleavage fracture criterion is as follows:
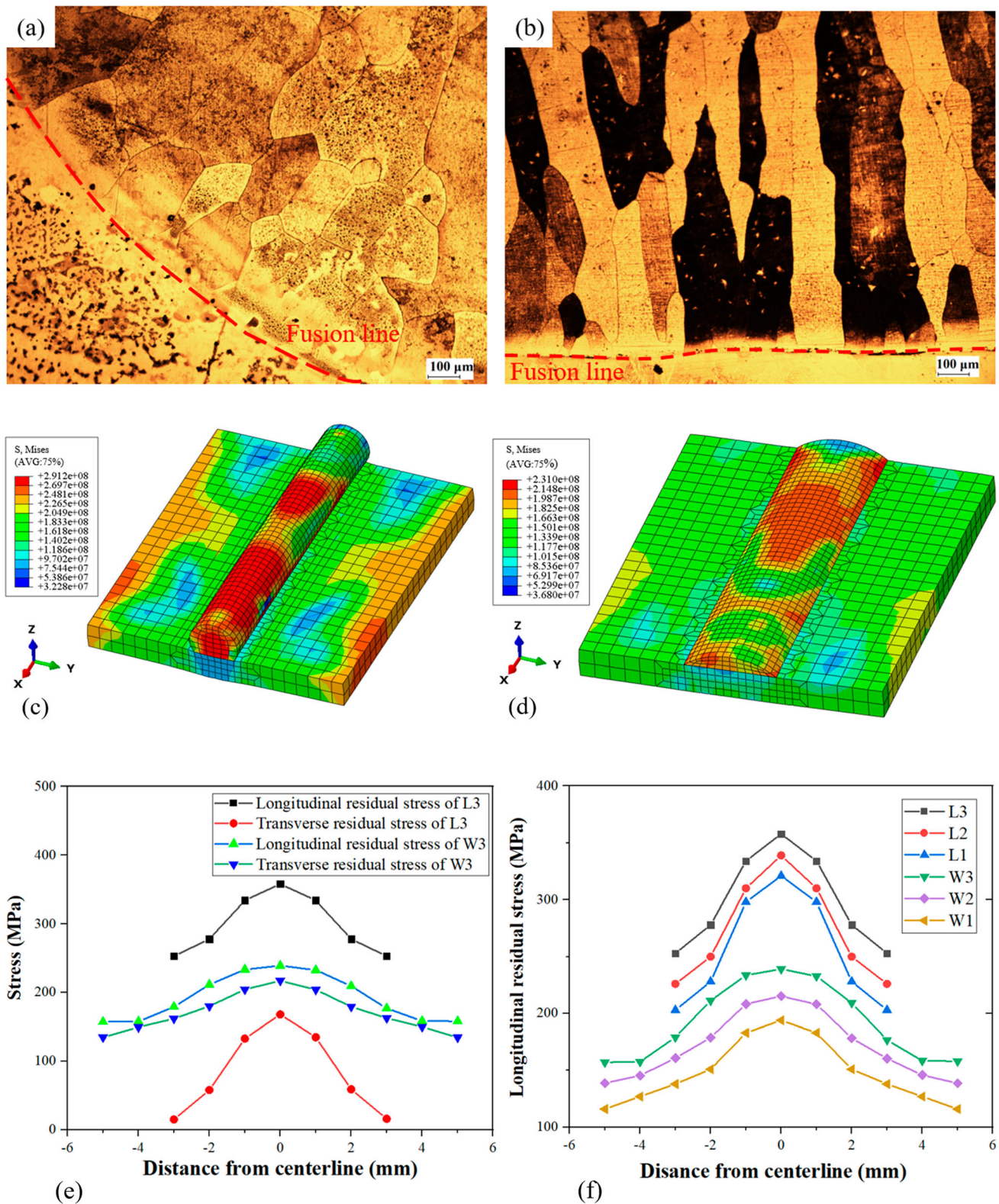


**Fig. 16** Microstructure at interface (a) line, (b) weave; Mises stress distribution diagram (c) line, (d) weave; (e) residual stress of Fe$_3$Al alloy at interface and (f) longitudinal residual stress of six samples

$$\sigma_c = \frac{2G\gamma_s}{k_y\sqrt{d}} \qquad\qquad (\text{Eq } 7)$$

where $\sigma_c$ is the stress required for crack propagation of grain diameter $d$, $d$ is the grain diameter, $G$ is the shear elastic modulus, $\gamma_s$ is the surface energy and $k_y$ is a constant related to the crystal type.

According to the above criteria, the smaller the grain size, the higher the fracture stress. Therefore, the refinement of microstructure at the interface caused by weaving is the metallurgical reason for the increase in the bonding strength.

As shown in Fig. 16(c) and (d) of simulated Mises stress diagrams after cooling, deposited layers are the stress concentration areas, and the maximum Mises stress in a straight line is higher than in weaving. The various temperature field distribution and thermal cycle curves as presented in Figs. 14 and 15 are precisely responsible for the distinct coupled stress field, the higher peak temperature and larger temperature gradient, the greater stress in the straight line path. The residual stress consists primarily of transverse residual stress and longitudinal residual stress, in which the longitudinal residual stress parallel to the deposited layer is the principal stress. Figure 16(e) illustrates the transverse and longitudinal residual stresses of the Fe$_3$Al alloy at the interface under two paths. Due to the narrow interface between the linear deposition layer and the substrate, the longitudinal residual stress in line way is much greater than the transverse residual stress.

Figure 16(f) shows that as current increases, residual stress increases correspondingly in both processes. This is mainly because the greater the current, the more heat is produced during arc deposition, and more residual stress is generated during cooling. Before measuring the bonding strength, the inherent brittle Fe$_3$Al alloy with high residual stress at the interface is a potential crack source, when conducting the test, the crack, in response to increasing compressive force, will nucleate and expand rapidly, and eventually form brittle cleavage fractures. According to the brittle crack propagation theory, when the local stress exceeds the critical stress after crack nucleation, crack propagation can occur in the matrix, which means that the larger the residual stress, the smaller the compressive force required for crack propagation. This is why the bonding strength decreases as the current increases as presented in Fig. 10(d).

## 5. Conclusions

In this study, two arc deposition methods were used to prepare Fe$_3$Al layers on steel plates by arc deposition technology. The influence of the two methods on the morphology, wettability and microstructure of the cladding were compared. A high-speed camera was used to capture the molten pool images in the formation process, the temperature fields and stress distribution of these two means were also simulated by FEA. The main conclusions are as follows:

1. Weave deposition methods are superior to linear deposition methods in terms of formability with a continuous and regular surface forming morphology, no pores and cracks, a low dilution rate ($< 10\%$) and small contact angles ($< 45°$).

2. The deposition layer formed by the two different deposition approaches is mainly composed of B2-FeAl phase and DO$_3$-Fe$_3$Al phase.

3. The weave arc molten pool velocity is 0.06 m/s, which is much greater than the linear molten pool velocity of 0.0033 m/s. The distinction between two means has primarily to do with the contrasting velocity of the molten pool, thus leading to the smaller volume of the molten pool and the smaller dilution rates in weave method. Combined with the high-speed camera results, the arc force is conducive to the spread of liquid metal, resulting in a relatively small contact angle in the weave arc deposition.

4. FEA reveals that the distribution of temperature field is quite different. According to the thermal cycle curve, the diverse grain morphologies in respective regions of two methods are due mainly to the variation of $G$ and $R$. Columnar to equiaxed transition occurred in both processes. The finer grain of varied regions in weave layer is mainly attributed to the faster cooling rate.

5. Compared to sample Line 1 formed in line, sample Weave 1 prepared in weaving has a bonding strength of 123.69 MPa, with a significant increase of 153.15%. The distribution of microstructure and the residual stress at the interface both have a considerable impact on the greater bonding strength of weave process.

## References

1. M. Palm, F. Stein, and G. Dehm, Iron Aluminides, *Annu. Rev. Mater. Res.*, 2019, **49**(1), p 297–326.
2. M. Zamanzade, A. Barnoush, and C. Motz, A Review on the Properties of Iron Aluminide Intermetallics, *Crystals (Basel)*, 2016, **6**(1), p 10.
3. I.S. Golovin, A. Emdadi, A.M. Balagurov, I.A. Bobrikov, and J. Cifre, Anelasticity of Iron-Aluminide Fe$_3$Al Type Single and Polycrystals, *J. Alloys Compd.*, 2018, **746**, p 660–669.
4. S.C. Deevi, Advanced Intermetallic Iron Aluminide Coatings for High Temperature Applications, *Prog. Mater. Sci.*, 2021, **118**, 100769
5. M. Rajabi, M. Shahmiri, and M. Ghanbari, The Influence of B and Zr Additions on Microstructure, Mechanical Properties and Oxidation Behavior of Cast Ternary Fe-Al-Cr Alloys, *Mater. Res. Express*, 2019, **6**(8), p 0865g7.
6. S. Alkan and H. Sehitoglu, Non-Schmid Response of Fe$_3$Al: The Twin-Antitwin Slip Asymmetry and Non-Glide Shear Stress Effects, *Acta Mater.*, 2017, **125**, p 550–566.
7. M. Zamanzade, H. Vehoff, and A. Barnoush, Cr Effect on Hydrogen Embrittlement of Fe$_3$Al-Based Iron Aluminide Intermetallics: Surface or Bulk Effect, *Acta Mater.*, 2014, **69**, p 210–223.
8. P. Kratochvil, M. Svec, R. Kral, J. Vesely, and P. Lukac, The Effect of Nb Addition on the Microstructure and the High-Temperature Strength of Fe$_3$Al Aluminide, *Metall. Mater. Trans. A*, 2018, **49A**(5), p 1598–1603.
9. Y. Chen, Z. Yao, P. Zhang, D. Wei, and X. Luo, First-Principles Study on Effects of Cr, Mo and W on the Electronic Structure and Mechanical Properties of FeAl Intermetallic Compounds, *Rare Metal Mater. Eng.*, 2014, **43**(9), p 2112–2117.
10. D. Hamana, L. Amiour, and M. Bouchear, Effect of Chromium Ternary Additions on the Ordering Behaviour in Fe-28 at.% Al Alloy, *Mater. Chem. Phys.*, 2008, **112**(3), p 816–822.

11. P. Kratochvil, P. Kejzlar, R. Kral, and V. Vodickova, The Effect of Zr Addition on the Structure and High Temperature Strength of Fe-30 at.% Al Type Alloys, *Intermetallics*, 2012, **20**(1), p 39–46.

12. Z. Mohammad, B. Afrooz, and M. Christian, A Review on the Properties of Iron Aluminide Intermetallics, *Crystals*, 2016, **6**(1), p 10.

13. C. Shen, K. Liss, Z. Pan, Z. Wang, and X. Li, Thermal Cycling of $Fe_3Al$ Based Iron Aluminide during the Wire-Arc Additive Manufacturing Process: An In-Situ Neutron Diffraction Study, *Intermetallics*, 2018, **92**, p 101–107.

14. C. Shen, Z. Pan, D. Cuiuri, J. Roberts, and H. Li, Fabrication of Fe-FeAl Functionally Graded Material using the Wire-Arc Additive Manufacturing Process, *Metall. Mater. Trans. B*, 2016, **47**(1), p 763–772.

15. L. Adler, Z. Fu, and C. Koerner, Electron Beam Based Additive Manufacturing of $Fe_3Al$ Based Iron Aluminides—Processing Window, Microstructure and Properties, *Mater. Sci. Eng. A*, 2020, **785**, 139369

16. P.O. Mohammadi, R. Raiszadeh, and H. Shahverdi, Formation of Iron Aluminide Coatings on Plain Carbon Steel by TIG Process, *Int. J. Adv. Manuf. Technol.*, 2018, **96**(5–8), p 1655–1663.

17. S. Xu, J. Wang, Z. Wang, Q. Sui, and F. Zhao, Microstructure and Mechanical Properties of $Fe_3Al$ Based Alloy Fabricated by Laser Metal Deposition, *Mater. Lett.*, 2022, **306**, 130919

18. Y. Li, H. Ma, and J. Wang, A Study of Crack and Fracture on the Welding Joint of $Fe_3Al$ and Cr18-Ni8 Stainless Steel, *Mater. Sci. Eng. A*, 2011, **528**(13–14), p 4343–4347.

19. C. Chen, J. Zhao, J. Zhou, and F. Xue, Fabrication of $Fe_3Al$ Cladding Layers by Cold Metal Transfer Arc Deposited Technique, *Mater. Res. Express*, 2019, **6**(11), p 116534.

20. Y.B. Lin, T.F. Chen, J. Tao, Y.Z. Shen, and H.G. Li, Diffusion and Plasma Oxidation Mechanism of Fe-Al Coatings, *Surf. Eng.*, 2015, **31**(5), p 329–334.

21. G. Yang, H. Wang, C. Li, and C. Li, Effect of Annealing on the Microstructure and Erosion Performance of Cold-Sprayed FeAl Intermetallic Coatings, *Surf. Coat. Technol.*, 2011, **205**(23–24), p 5502–5509.

22. X. Luo, J. Cao, G. Meng, Y. Chuan, and Z. Yao, Systematical Investigation on the Microstructures and Tribological Properties of Fe-Al Laser Cladding Coatings, *Appl. Surf. Sci.*, 2020, **516**, 146121

23. S. Yang, J. Zhang, J. Lian, and Y. Lei, Welding of Aluminum Alloy to Zinc Coated Steel by Cold Metal Transfer, *Mater. Des.*, 2013, **49**, p 602–612.

24. A. Evangeline and P. Sathiya, Cold Metal Arc Transfer (CMT) Metal Deposition of Inconel 625 Superalloy On 316L Austenitic Stainless Steel: Microstructural Evaluation, Corrosion and Wear Resistance Properties, *Mater. Res. Express*, 2019, **6**(6), p 66516.

25. H. Zhang, S. Hu, Z. Wang, and Y. Liang, The Effect of Welding Speed on Microstructures of Cold Metal Transfer Deposited AZ31 Magnesium Alloy Clad, *Mater. Des.*, 2015, **86**, p 894–901.

26. G. Mou, X. Hua, D. Wu, Y. Zhang, and D. Wang, Study on Weld Seam Surface Deposits of $CuSi_3$ CMT Brazing, *Int. J. Adv. Manuf. Technol.*, 2017, **92**(5–8), p 2735–2742.

27. A. Benoit, P. Paillard, T. Baudin, V. Klosek, and J.B. Mottin, Comparison of Four Arc Welding Processes Used for Aluminium Alloy Cladding, *Sci. Technol. Weld. Join.*, 2015, **20**(1), p 75–81.

28. C. Shen, Z. Pan, D. Cuiuri, D. Ding, and H. Li, Influences of Deposition Current and Interpass Temperature to the $Fe_3Al$-Based Iron Aluminide Fabricated using Wire-Arc Additive Manufacturing Process, *Sci. Technol. Weld. Join.*, 2017, **88**(5–8), p 2009–2018.

29. J. Goldak, A. Chakravarti, and M. Bibby, A New Finite Element Model for Welding Heat Sources, *Metall. Trans. B*, 1984, **15**(2), p 299–305.

30. A.S. Azar, S.K. Ås, and O.M. Akselsen, Determination of Welding Heat Source Parameters from Actual Bead Shape, *Comput. Mater. Sci.*, 2012, **54**, p 176–182.

31. K. Oyama, S. Diplas, M. M'Hamdi, A. Gunnæs, and A.S. Azar, Heat Source Management in Wire-Arc Additive Manufacturing Process for Al-Mg and Al-Si Alloys, *Addit. Manuf.*, 2019, **26**, p 180–192.

32. Y. Li, C. Xia, and J. Wang, Stress Distribution Near the Diffusion Bonding Interface of $Fe_3Al$ and Cr18-Ni8 Stainless Steel, *Met. Mater.*, 2012, **50**(3), p 214–219.

33. Y. Chen, Y. He, H. Chen, H. Zhang, and S. Chen, Effect of Weave Frequency and Amplitude on Temperature Field in Weaving Welding Process, *Int. J. Manuf. Technol.*, 2014, **75**(5–8), p 803–813.

34. S. Kou, *Welding Metallurgy*, John Wiley & Sons Inc, New York, 2003